Microstructural Analysis of Ti-10V-2Fe-3Al Examining Effects of an Added Beta Stabilizer

Thesis

Presented in Partial Fulfillment of the Requirements for the Degree Master of Science in the Graduate School of The Ohio State University

By

Katherine Rashedi

Graduate Program in Materials Science and Engineering

The Ohio State University

2023

Thesis Committee

Dr. Hamish L. Fraser, Advisor

Dr. Gopal B. Viswanathan

Abstract

Ti-10V-2Fe-3Al (Ti-1023) is a near beta titanium alloy. It is commonly used in airframes and landing gear due to its high fatigue life, high strength, and deep hardenability. Titanium alloy components for aerospace applications can be produced using additive manufacturing (AM), however, as-deposited Ti alloys typically form columnar grains parallel to the build direction resulting in anisotropic properties. Previous research has shown that the addition of beta eutectoid stabilizers to Ti alloys can promote an equiaxed grain structure in AM depositions by increasing the freezing range.

In this research, the effect of adding Fe, a beta eutectoid stabilizer, to Ti-1023 was studied to determine its influence on the freezing range, grain morphology and α-lath structure. ThermoCalc was used to predict the freezing range of Ti-1023 with Fe additions of up to 3 wt.%. The freezing range increased from 79°C for Ti-1023 to 149°C for Ti-1053 (3 wt% Fe addition). Samples were produced by vacuum arc melting to determine the effect of Fe on the grain morphology. The aspect ratio was similar for all compositions, however, the average grain size decreased with increasing Fe additions. Heat treatments were performed on the alloys and compared to other Ti alloys with a similar molybdenum equivalency. It was determined that the α-lath thickness can be modified by varying the heating rate to the aging temperature.

Dedication

Dedicated to my family and friends for their continuous love and support

Acknowledgments

I would like to express my sincerest gratitude to my advisor, Professor Hamish Fraser, for giving me the opportunity to be a part of CAMM. I will always value the experiences and learning opportunities I have had as a graduate student at CEMAS. I would like to extend a huge thank you to Brian Welk for his mentorship in all aspects of my career. I would not be where I am today without his guidance and support. I would also like to thank Dr. Sam Kuhr and Professor Babu Viswanathan for their advice and encouragement over the years. Lastly, I would like to thank other current and former Fraser group members for their guidance, but more importantly, their friendship: Dr. Nevin Taylor, Dr. Zak Kloenne, Dr. Calvin Mikler, and Mathew Cohen.

Vita

2016………………………...…………….Avon High School

2020……………………………………....B.S. Department of Materials Science and Engineering, The Ohio State University

2020 – Present………………………………Graduate Research Associate, Department of Materials Science and Engineering, The Ohio State University

Fields of Study

Major Field: Materials Science and Engineering

Table of Contents

List of Tables

List of Figures

Chapter 1. Introduction

1.1 Titanium History

In 1791 William Gregor discovered an unknown element. In 1795 Martin Heinrich Klaproth identified the same unknown element in the form of an oxide and named it Titanium. It wasn't until 1910 that Matthew Albert Hunter isolated titanium from its ore. In 1940, the Hunter process was replaced by the Kroll process which was more economically attractive. Kroll developed a commercial process to extract titanium from its ore using magnesium as the reducing agent [1][2]. The Kroll process involves reducing titanium tetrachloride to produce titanium sponge [3]. The Kroll process is still used today with only minor modifications.

Titanium alloys became important for aircraft engines after World War II [2]. The aerospace industry is currently the most common application for titanium and titanium alloys. Seventy two percent of United States titanium production is used in the aerospace market [3]. Ti64 began being used in the United States in 1954 and remains the most used titanium alloy today. Figure 1 shows that Ti64 accounted for 56% of the US titanium market in 1998, which is more than all other titanium alloys and CP-Ti combined. As titanium alloys were developed, there was also a focus on CP-Ti for its corrosion resistance which is often useful in non-aerospace applications [1].

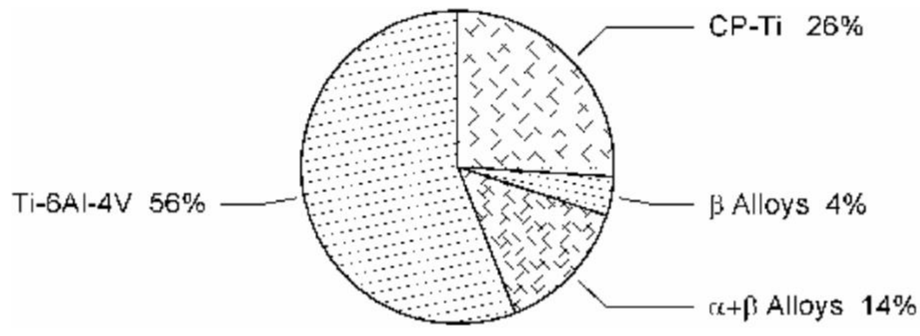

Figure 1: USA titanium market breakdown, 1998 [1]

1.2 Titanium Classification

Titanium alloys can be classified into three main groups based on their alloying elements and stable phases – alpha and near alpha alloys, alpha/beta alloys, and metastable beta alloys. In commercially pure titanium, there is a transition at 882°C from hexagonal close packed (hcp) alpha in the lower temperature region to body centered cubic (bcc) beta at higher temperatures [1]. The addition of alloying elements can change the α/β transition temperature. Elements that increase the transition temperature are called alpha stabilizers and include Al, O, N, and C. Alloying elements that decrease the transition temperature are beta stabilizers and can be divided into two groups, beta isomorphous elements and beta eutectoid elements. V, Mo, and Nb are common beta isomorphous elements, while Cr, Fe, Si, and Ni are common of beta eutectoid elements. There are also neutral alloying elements that don't have an effect on the transition temperature [1][4]. Figure 2 illustrates the effect of each group of alloying elements on a titanium phase diagram. The pseudo-binary phase diagram in Figure 3 shows the phase boundaries for each classification of alloy with increasing amounts of beta stabilizers. Additionally, the beta stability of a titanium alloy can be determined with the molybdenum equivalency equation: Mo Eq = 1.0Mo + 0.67V + 0.44W + 0.28Nb + 0.22Ta + 1.6Cr + 2.9Fe + 1.7Co – 1.0Al [5]. This equation weighs each alloying element differently based on their strength as a beta stabilizer.

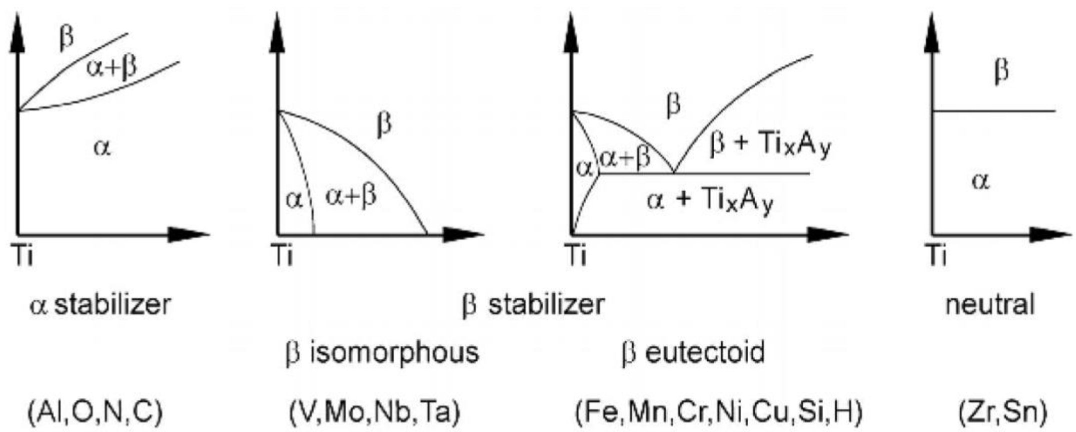

Figure 2: Titanium alloying elements effect on phase diagrams [1]

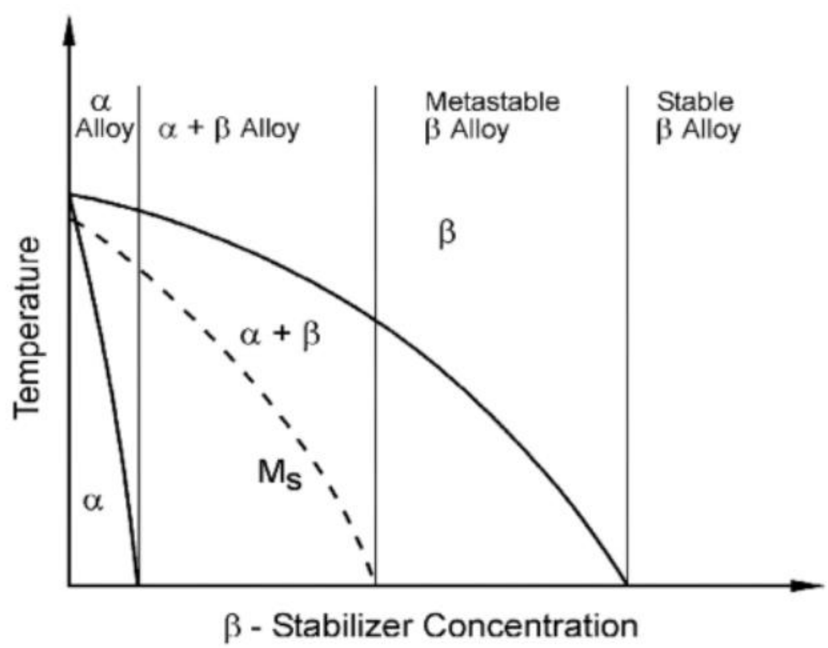

Figure 3: Pseudo-binary isomorphous phase diagram [1]

1.2.1 α and Near α Alloys

Alpha and near alpha alloys include CP Ti and titanium alloys that primarily contain the alpha phase with a very small amount of the beta phase. CP Ti is commonly used in chemical processing equipment and piping applications because of its excellent corrosion resistance from the passive oxide layer formed [1]. Alpha titanium alloys also have excellent corrosion resistance but have a higher strength from added solid solution strengtheners compared to CP Ti. Alpha titanium alloys have been used for cryogenic tanks in spacecrafts due to their weldability and ductility at cryogenic temperatures [1].

1.2.2 α/β Alloys

These alloys contain alpha stabilizers to stabilize and strengthen the alpha phase, as well as 4-6% of beta stabilizers. For each alloy, various microstructures can be obtained by changing the processing conditions. Lamellar, equiaxed, and bi-modal structures, which contain equiaxed primary alpha in a lamellar α/β matrix, can be produced [1]. Ti-6V-4Al, an α/β alloy, accounts for over 50% of all commercially used titanium alloys [6]. Ti-64 is commonly used for aircraft structural parts due to its high yield stress and fatigue strength. Compared to its competitor high strength aluminum, it has better corrosion resistance, higher elastic modulus, and a higher temperature capability. Another common application is both rotating and non-rotating parts in aero-engines [1].

1.2.3 Metastable β Alloys

The metastable beta phase is produced because these alloys don’t transform to martensite upon quenching. Heat treatments are done to precipitate the alpha phase. Metastable beta alloys are often referred to as either high strength beta alloys which contain a higher volume fraction of alpha or heavily stabilized beta alloys which contain a lower volume fraction of the alpha phase [1]. Examples of alloys in these two groups are Ti-10Al-2Fe-3V and Ti-21S respectively. The use of beta alloys has been increasing over the years due to their advantages over α/β alloys including their higher yield stress, lower processing temperatures, and higher tolerance to hydrogen[1].

1.3 β Titanium in the Aerospace Industry

While β titanium has only a small share of the titanium market (4%), it has a heavier use in the aerospace industry [1]. The use of β titanium in aerospace applications is increasing with the use of Ti-64 decreasing. Ti-10-2-3 is commonly used for landing gear on aircrafts [7]. The high volume of Ti-10-2-3 used in landing gear eventually led to the volume of β titanium alloys outnumbering the volume of Ti-64 for the first time on a commercial airplane on the Boeing 777 aircraft [1]. Ti-15-3, a heavily stabilized beta titanium alloy, is used for nut clips on aircrafts. This alloy is more attractive that previously used steel because of its corrosion resistance. A variety of springs used on airplanes are made of Ti-15-3 or Beta C. Titanium springs can decrease the weight of the springs by up to 70% compared to steel springs. They are also used for their low modulus of elasticity and high yield strength. β21S is used in the nacelle structure of aero engines for its oxidation resistance [1][8].

1.3.1 Ti-10V-2Fe-3Al

Ti-10-2-3 is a near beta alloy consisting of 10V, 2Fe, and 3Al. Ti-10-2-3 is commonly processed by beta forging followed by alpha + beta forging to plastic strains of 15-25% and a heat treatment to produce a bimodal structure [1]. It is commonly used in airframes and landing gear and is desirable due to its high fatigue life, high-strength, and deep hardenability [7].

1.3.2 β21S

TIMETAL 21S is a metastable beta alloy. It's used for its oxidation resistance, high temperature strength, and creep resistance [8]. Ti21S was developed for use as a foil in metal matrix composites [2]. In addition to metal matrix composites, typical applications include the warm airframe of an engine structure, fasteners, and castings [8].

1.4 Scheil Solidification

Various models can be used to illustrate an alloy's cooling. Equilibrium cooling is slow enough to provide time to reach equilibrium, so the solid and liquid compositions follow the lever rule at any given temperature. The Scheil-Gulliver equation is commonly used to model solidification in additive manufacturing and is represented by the following: $C_L = C_o(f_L)^{k-1}$and $C_s = kC_o(1 - f_s)^{k-1}$ where C_L and C_s are the concentration of the solute in the liquid and solid, C_0 is the nominal fluid concentration, $f_s$and $f_L$are the fraction of solid and liquid, and $k = \frac{C_s}{C_L}$ is the partition coefficient [9]. In the Scheil equation, it is assumed that there is no diffusion in solid, infinite diffusion in liquid, and local equilibrium exists at the solid-liquid interface. As the solid forms, the solute is rejected into the liquid; The liquid then becomes enriched with solute [10]. In this model, the liquid could possibly reach the eutectic composition. Actual alloy solidification is usually somewhere between the two models.

1.5 Motivation

Additively manufactured titanium alloys typically produce long columnar grains resulting in anisotropic properties. The addition of a beta stabilizer has been shown to expand the freezing range for the alloy resulting in an equiaxed grain structure. This research studies the effect of adding Fe, a beta eutectoid stabilizer, to Ti-1023 to determine its influence on the freezing range, grain morphology and α-lath structure.

Chapter 2. Experimental Procedure

2.1 ThermoCalc and Arc Melting

ThermoCalc was used to perform phase diagram calculations and classic Scheil solidification simulations for each alloy to illustrate the effect of adding increasing amounts of iron, a beta stabilizer, to Ti 10-2-3 on the alloys' solidification range. Ti 10-2-3 with additions of 1, 2, and 3 weight percent iron were chosen to study. Twenty-five-gram buttons of these alloys were produced using an arc-melter. The arc-melter was operated under vacuum with a partial pressure of Argon to avoid atmospheric contamination. The arc-melted buttons were melted three times each and flipped between each melt to ensure homogeneity. The desired alloys were made using pre-made Ti 10-2-3 and iron powder. Molybdenum equivalency values were calculated for all compositions of the arc-melted alloys as well as other common β-Ti alloys. The alloy TIMETAL 21S was chosen to study because it has a comparable β-phase stability to Ti 10-2-3 +1 wt.% Fe.

2.2 Heat Treatments

The various alloys were solutionized above their beta transus temperatures at 880 °C for 30 min and water quenched. Samples of each were aged at 600 °C for 2 hours followed by a water quench. A second set of samples followed the same heat treatment but were placed in a room temperature furnace and were heated at a rate of 5C/min up to 600 °C with a 2-hour hold. Figure 4 shows a schematic diagram of the heat-treatment process.

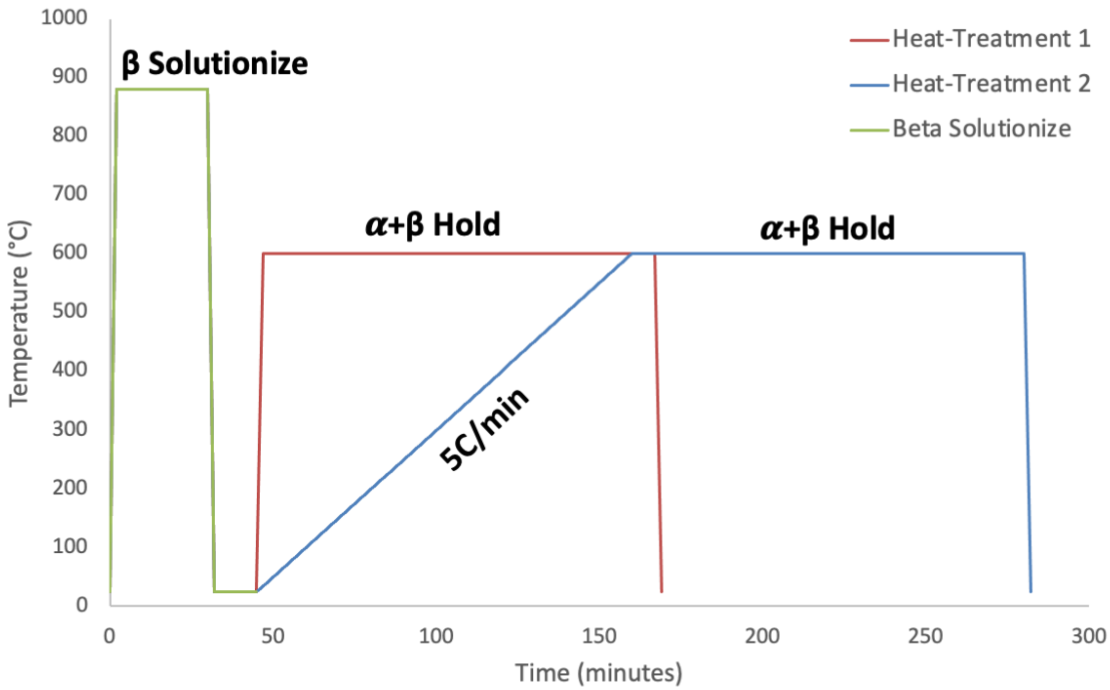

Figure 4: Schematic diagram of heat treatment process

2.3 Sample Preparation

Samples for heat treatments were cut using wire electrical discharge machining (EDM). Post-heat-treated samples were cut in half to eliminate any alpha case on the face of the sample that would be viewed. Samples were then mounted in conductive bakelite and polished using 400, 600, and 800 grit SiC paper, followed by 6um and 1um diamond solution and 0.05um colloidal silica. Samples were cleaned in an ultrasonic bath and scrubbed under running water with a cotton ball. Samples that were imaged with an optical microscope were etched using Kroll's Reagent.

2.4 Scanning Electron Microscope Characterization

A set of samples were imaged prior to heat treatment with optical microscopy on the Olympus DSX 510. The stitching software was used to image large areas. The heat-treated samples were characterized using an Apreo (Thermo Fisher Scientific) scanning electron microscope (SEM) using a 5kV accelerating voltage, 3.2nA beam current, and the T1 backscattered electron detector. MIPAR image analysis software was used to determine the alloys' phase fractions, areal number density of alpha precipitates, and alpha lath width.

Chapter 3. Results and Discussion

3.1 ThermoCalc Solidification Range Predictions

ThermoCalc was used to illustrate the impact the alloying addition, Fe, has on the freezing range of Ti 10-2-3. The phase diagram in Figure 5a shows Ti-10V-3Al with increasing amounts of Fe. The results show that the freezing range widens with increasing Fe. Scheil solidification diagrams were also examined for the same compositions since the Scheil equation may be a more accurate predictor of solidification in additive manufacturing. Figure 5b shows a plot of solidification range as a function of weight percent iron for both the Scheil equation and equilibrium prediction methods. While the equilibrium freezing range continues to increase with increasing iron, the Scheil prediction shows that the freezing range peaks between 1 and 2 weight percent Fe. This is likely because of the prediction of a Ti-Fe intermetallic. With more Fe the formation of the intermetallic would happen at higher temperatures so therefore the freezing range appears to decrease. When enough of a beta stabilizing element is added the freezing range peaks. Although, the Scheil equation begins to break down as it assumes too much diffusion in the liquid. The actual freezing ranges are likely somewhere between the two models.

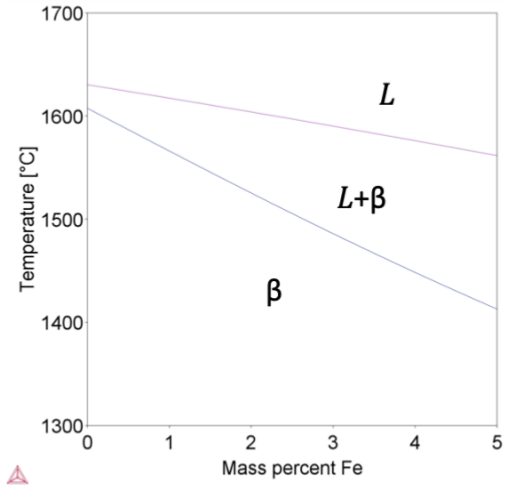

a)

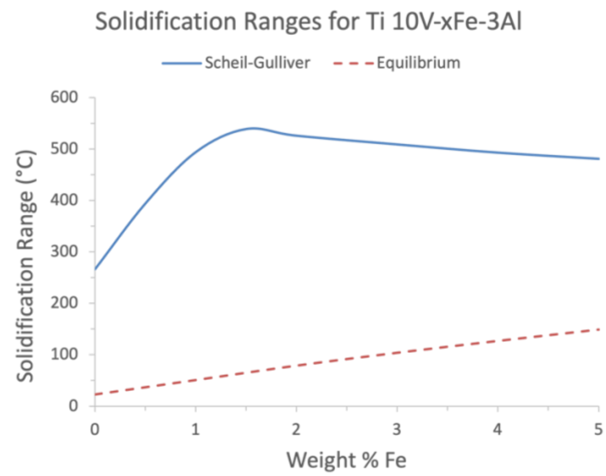

b)

Figure 5: a) Pseudo-binary phase diagram calculated using Thermo-Calc Software for Ti1023-Fe; b) Plot of Scheil and Equilibrium solidification ranges.

3.2 Grain Analysis of Arc Melted Buttons

MIPAR was used to analyze the beta grain size and morphology of the arc melted buttons. Figure 6 shows a sample of each alloy with the grain boundaries highlighted and the grains colored according to their area. The top edge of each sample contains smaller grains because the top of the arc melted button cools faster. This effect seems to be stronger in the alloys with additions of 2 and 3wt.% Fe.

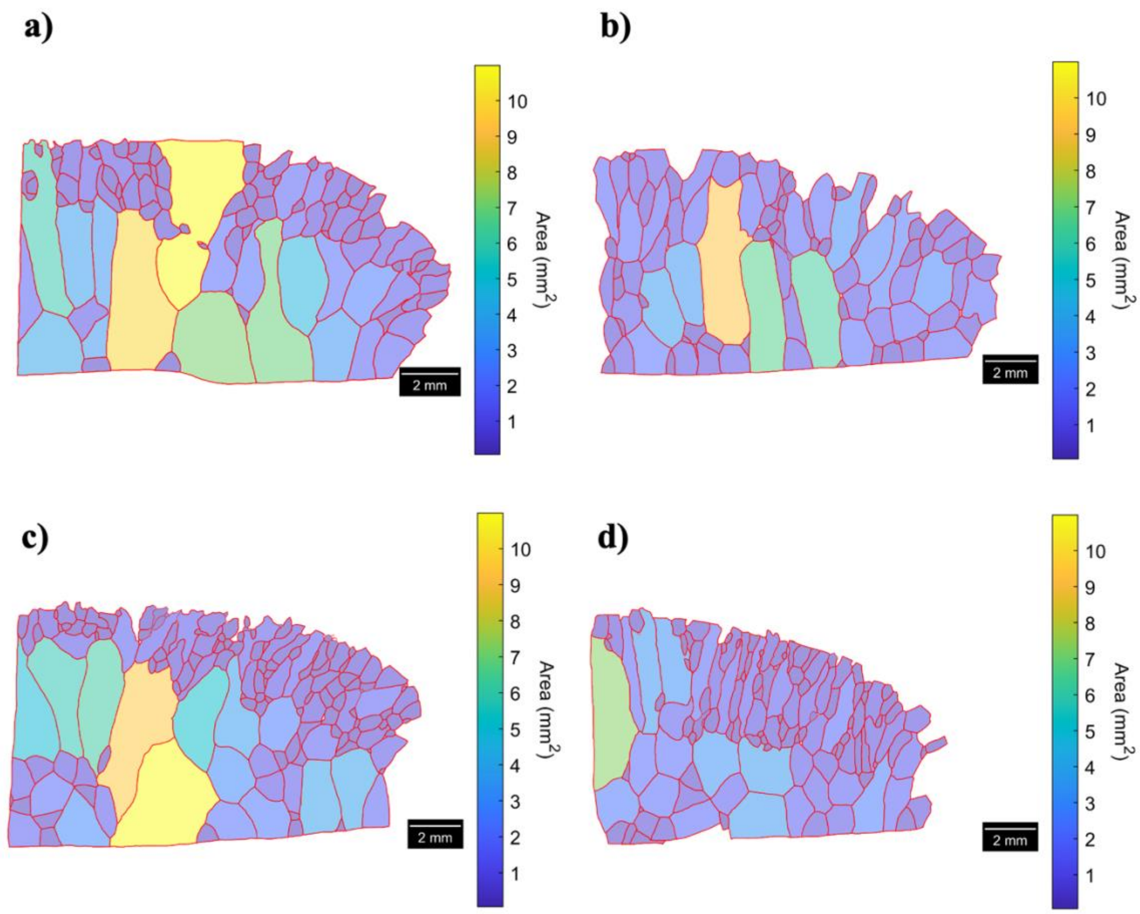

Figure 6: MIPAR grain size map of arc melted buttons a) Ti-10V-2Fe-3Al b) Ti-10V-3Fe-3Al c) Ti-10V-4Fe-3Al d) Ti-10V-5Fe-3Al

Table 1 shows that the average beta grain areas for Ti-10V-2Fe-3Al, Ti-10V-3Fe-3Al, Ti-10V-4Fe-3Al, and Ti-10V-5Fe-3Al were 0.97±1.88 mm^2, 1.03±1.40 mm^2, 0.77±1.53 mm^2, 0.69±0.97 mm^2 respectively. Overall, there is a decrease in average grain size. The alloy with the addition of 3wt.% Fe also has the smallest standard deviation. Table 2 shows the average aspect ratios for the beta grains in each alloy. Although there is no clear trend with the addition of iron, all the alloys appear to on average have equiaxed grains as the aspect ratio is less than 3.

Table 1: Average grain sizes of arc melted buttons calculated with MIPAR

	Grain Area (mm^2)			
	Ti1023	Ti1023+1Fe	Ti1023+2Fe	Ti1023+3Fe
Average	0.97	1.03	0.77	0.69
Standard Deviation	1.88	1.40	1.53	0.97
Max	10.99	9.35	10.98	7.32
Min	0.00	0.01	0.01	0.01

Table 2: Average grain aspect ratio of arc melted buttons

	Grain Aspect Ratio			
	Ti1023	Ti1023+1Fe	Ti1023+2Fe	Ti1023+3Fe
Average	2.1	2.5	2.2	2.7
Standard Deviation	1.0	1.4	1.1	1.6
Max	7.7	7.4	8.9	10.2
Min	1.0	1.0	1.1	1.1

3.3 Heat Treatment Study

Heat treatments were conducted on the various alloys to understand how the microstructure changes with the addition of Iron. All samples were solutionized at 880°C for 30 minutes followed by a water quench. The 2-hour age at 600°C will be referred to as HT1. The 5°C/min ramp up rate to 600°C, held for 2 hours, and water quenched will be referred to as HT2. Figure 7 and Figure 8 show SEM backscattered images of samples that had undergone HT1. Figure 9 shows images of samples that had undergone HT2. Upon examining the images, it is noticeable that HT2 produced much less variation in phase fraction and alpha lath width. Table 3 shows the alpha lath area fraction, number density, and width for each sample which were calculated using MIPAR. For both heat treatments, with the addition of Fe the alpha area fraction decreased as Fe is a beta stabilizer. The alpha lath number density was roughly similar for all alloys and was about 5 laths/μm^2. For HT1 the alpha lath width increases with increasing Fe content, while the alpha lath width decreased with increasing Fe content for HT2. Ti-10V-5Fe-3Al had an alpha lath width of 106nm for HT1 and 58.5 for HT2. Data for Ti 21S HT2 is not shown as the alpha was so fine that an SEM image clear enough for MIPAR analysis was not able to be obtained. Ti 21S is closest in moly equivalency to Ti-10V-3Fe-3Al, but closest in phase fractions to Ti-10V-5Fe-3Al. This alloy also produced a much finer alpha lath compared to the others.

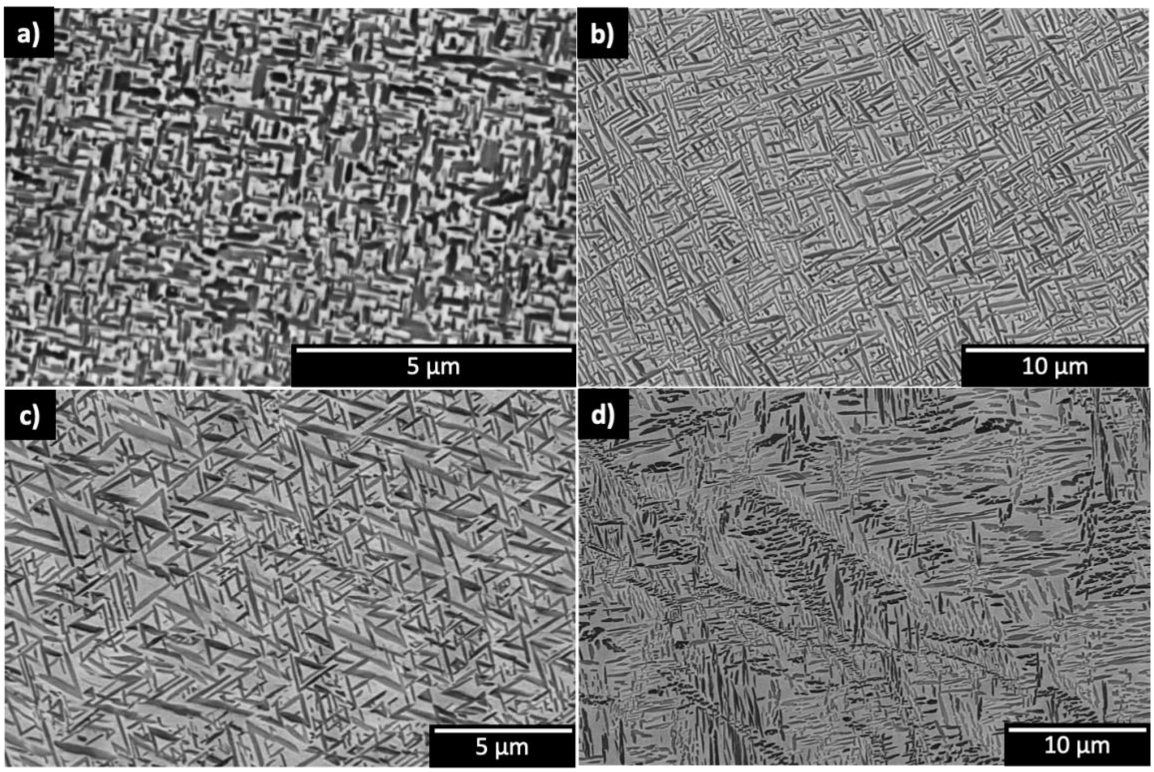

Figure 7: T1 detector SEM images of alloys solutionized at 880°C for 30 minutes and water quenched, then heat treated at 600°C for 2 hours followed by a water quench; a) Ti-10V-2Fe-3Al b) Ti-10V-3Fe-3Al c) Ti-10V-4Fe-3Al d) Ti-10V-5Fe-3Al

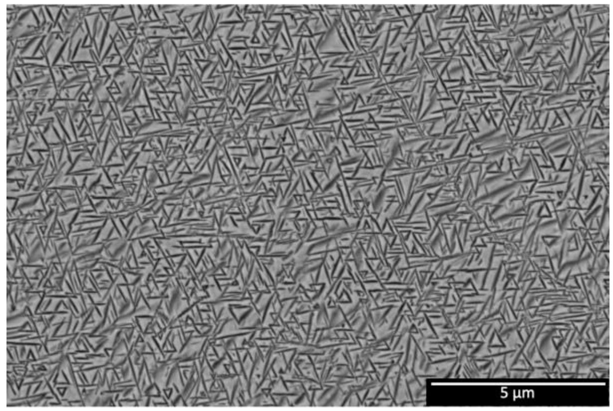

Figure 8: T1 detector image of Ti 21S solutionized at 880°C for 30 minutes and water quenched, then heat treated at 600°C for 2 hours followed by a water quench

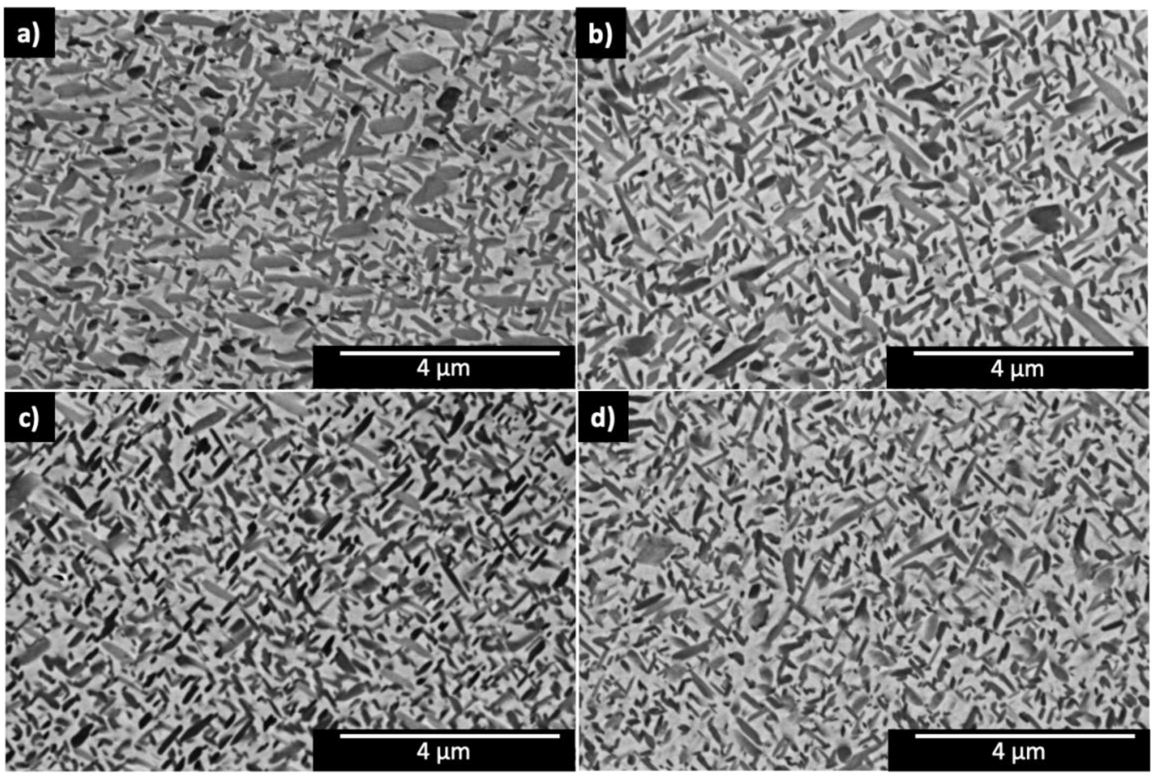

Figure 9: T1 detector SEM images of alloys solutionized at 880°C for 30 minutes and water quenched, then heated to 600°C at a rate of 5°C/min and held for 2 hours followed by a water quench; a) Ti-10V-2Fe-3Al b) Ti-10V-3Fe-3Al c) Ti-10V-4Fe-3Al d) Ti-10V-5Fe-3Al

Table 3: Alpha lath area fraction, number density, and width of heat treated alloys calculated via MIPAR

	Alpha Area Fraction (%)		Alpha Lath Number Density (features/um^2)		Alpha Lath Width (nm)	
Sample	HT1	HT2	HT1	HT2	HT1	HT2
Ti1023	51.2	49.8	2.4	3.8	61.4	64.5
Ti1023+1Fe	48.8	46.5	0.9	4.3	90.4	65.1
Ti1023+2Fe	44.7	43.7	4.5	7.6	82.2	58.5
Ti1023+3Fe	39.2	42.3	3.2	7.3	106.0	58.5
Ti 21S	38.5		5.5		43	

3.4 Accelerating Voltage Comparison in β21S

The SEM accelerating voltage typically used for Ti alloys and used for most images in this document is 5kV. It is important to understand changing the SEM imaging parameters can change how the microstructure appears in the image, and therefore changes the phase fractions calculated from the images. Figure 10 shows four T1 detector images of the same area on a sample of Ti 21S which had undergone the same heat-treatment as HT1 but with only a 20min age. The four images were taken at 20kV, 10kV, 5kV, and 2kV. In the 20kV image, the edges of the alpha laths are more diffuse compared to the 10kV and 5kV images. This would cause a large amount of uncertainty in determining the amount of alpha and beta phases. Additionally, the 2kV image shows a noticeable difference in the number of alpha laths as more appear in this image.

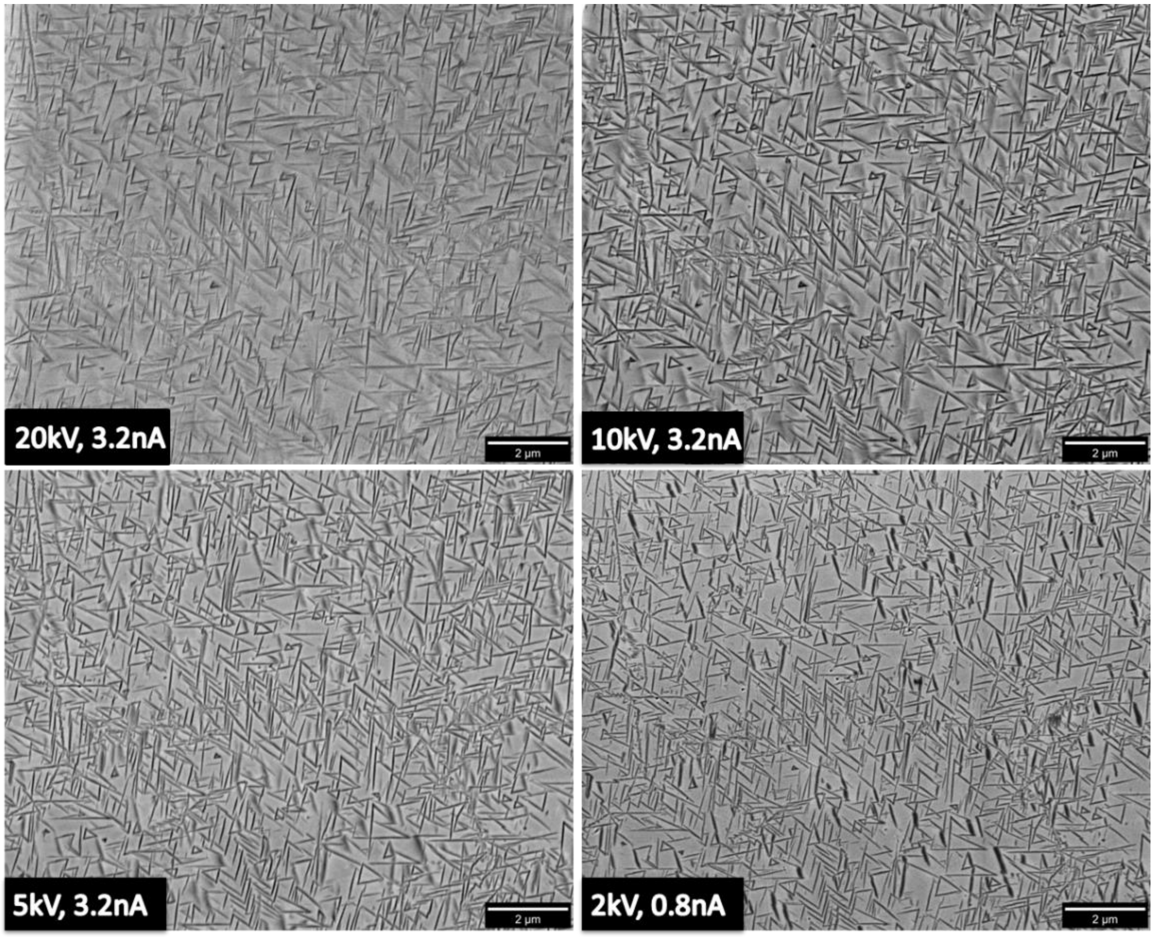

Figure 10: T1 detector SEM images of Ti 21S heat treated with HT1 taken of the same area at varying accelerating voltages

Figure 11 shows images of the same area at 20kV and 2kV. The red circles highlight a complete change in visible laths. MIPAR was used to threshold the alpha laths and subtract the alpha in the 20kV image from the alpha in the 2kV image. The resulting image is shown in Figure 12. The highlighted laths only appear at the low accelerating voltage. The calculated alpha volume fractions for the images at each accelerating voltage are displayed in Table 4. From 20kV to 2kV, the alpha volume fraction increases from 26.3% to 29.1%. The highlighted alpha laths in Figure 12 measure 4.5%. One might assume that at a lower accelerating voltage, the alpha volume fraction would decrease as there is a smaller interaction volume. The data for this sample shows that the alpha volume fraction increases at a lower accelerating voltage. This indicates that the deeper laths seen in the 20kV image are also intersecting with the surface so the 2kV image is picking up those same laths plus additional laths that only lie near the surface.

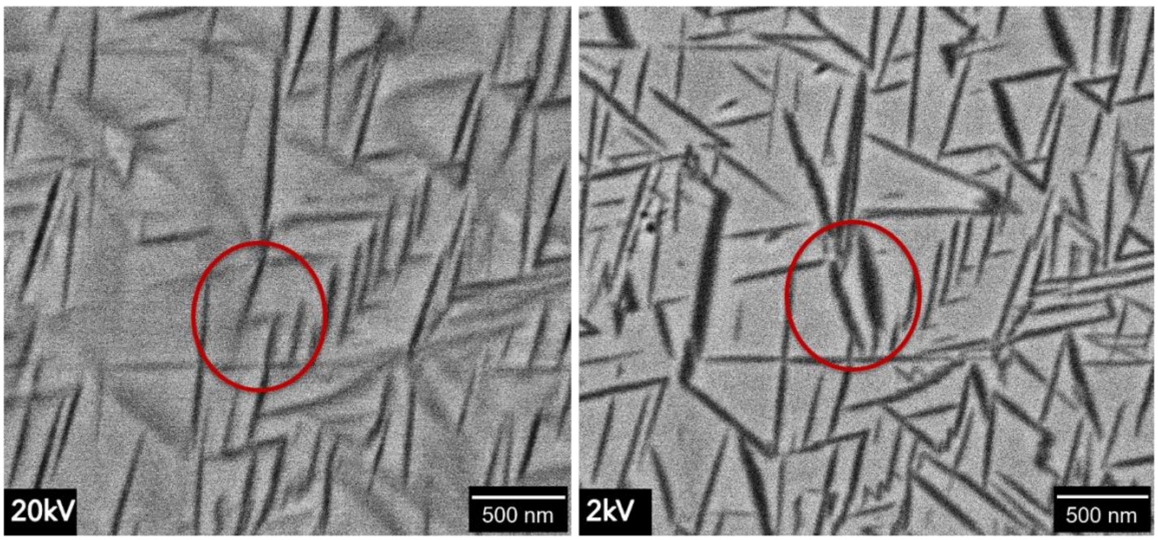

Figure 11: T1 SEM image showing difference in alpha laths detected by 20kV and 2kV

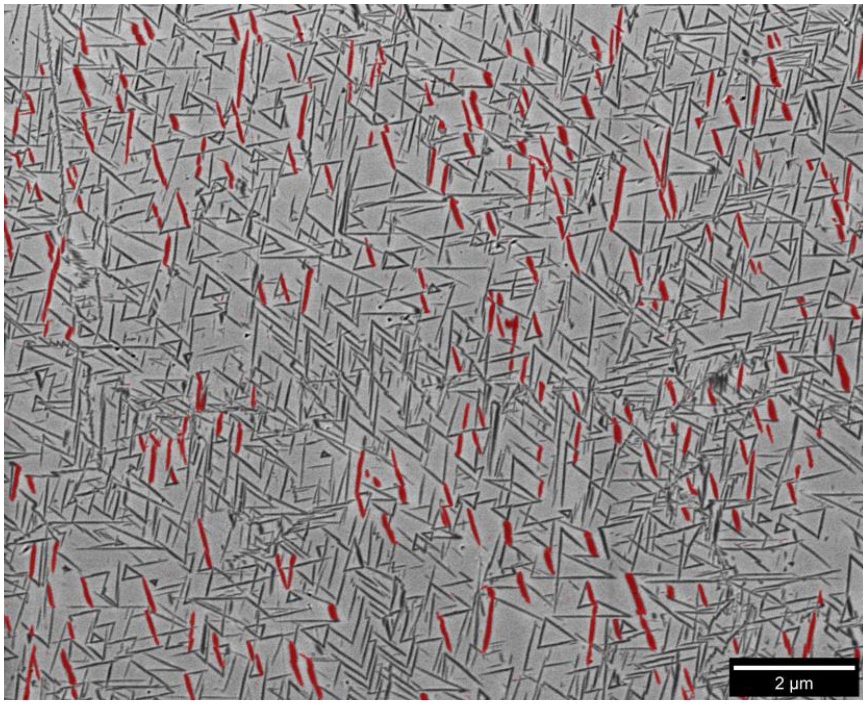

Figure 12: SEM image of Ti 21S taken at 2kV with alpha laths that aren't visible at 20kV highlighted

Table 4: Alpha volume fraction of Ti 21S for varying accelerating voltages

Accelerating Voltage	Alpha Volume Fraction (%)
20kV	26.3
10kV	25.9
5kV	30.7
2kV	29.1
surface laths at 2kV	4.5

Chapter 4. Summary and Future Work

4.1 Summary

The ThermoCalc simulation section of this study illustrated that the freezing range of Ti-10V-2Fe-3Al does increase with the addition of the beta stabilizer, Fe. The freezing range increased from 79°C for Ti-1023 to 149°C for Ti-1053. The grain aspect ratios of the arc melted buttons were similar for all compositions, however, the average grain size decreased with increasing Fe additions. The heat treatment study showed that the heat treatment with the 5°C/min ramp up rate produced a finer microstructure. While Ti 21S is closest in moly equivalency to Ti-10V-3Fe-3Al, it was closest in phase fraction to Ti-10V-5Fe-3Al, but ultimately the microstructure didn't resemble any of the other alloys as it produced a much finer alpha lath. Lastly, the accelerating voltage comparison illustrated the effects of interaction volume on the image produced. This demonstrated the need to use consistent accelerative voltages when comparing microstructures from multiple images.

4.2 Future Work

The ThermoCalc simulations showed an expanded freezing range so a LENS build could be made of Ti-10V-2Fe-3Al with increasing amounts of Fe to determine if there is a columnar to equiaxed transition. Additionally, more work needs to be done to determine how to properly image the Ti 21S alloy that had undergone HT2.

References

[1] Lütjering, G. and Williams, J.C., *Titanium*, 2nd ed. Berlin, Heidelberg: Springer, 2007. doi: 10.1007/978-3-540-73036-1.

[2] C. Leyens and M. Peters, Eds., *Titanium and Titanium Alloys: Fundamentals and Applications*, 1st ed. Wiley, 2003. doi: 10.1002/3527602119.

[3] M. R. Earlam, "Chapter 6 - The Kroll process and production of titanium sponge," in *Extractive Metallurgy of Titanium*, Z. Z. Fang, F. H. Froes, and Y. Zhang, Eds. Elsevier, 2020, pp. 97–112. doi: 10.1016/B978-0-12-817200-1.00006-5.

[4] B. A. Welk, "Microstructural and Property Relationships in Β-Titanium Alloy Ti-5553," 2010.

[5] I. Weiss and S. L. Semiatin, "Thermomechanical processing of beta titanium alloys—an overview," *Mater. Sci. Eng. A*, vol. 243, no. 1, pp. 46–65, Mar. 1998, doi: 10.1016/S0921-5093(97)00783-1.

[6] M. Peters, J. Hemptenmacher, J. Kumpfert, and C. Leyens, "Structure and Properties of Titanium and Titanium Alloys," in *Titanium and Titanium Alloys*, Wiley, 2003, pp. 1–36. [Online]. Available: https://onlinelibrary.wiley.com/doi/book/10.1002/3527602119

[7] "TIMETAL 10-2-3." Titanium Metals Corporation, 2000. [Online]. Available: https://www.timet.com/assets/local/documents/datasheets/metastablebetaalloys/10-2-3.pdf

[8] "TIMETAL 21S." Titanium Metals Corporation, 2000. [Online]. Available: https://www.timet.com/assets/local/documents/datasheets/metastablebetaalloys/21S.pdf

[9] C. J. Farnin, J. M. Rickman, and J. N. DuPont, "Solutions to the Scheil Equation with a Variable Partition Coefficient," *Metall. Mater. Trans. A*, vol. 52, no. 12, pp. 5443–5448, Dec. 2021, doi: 10.1007/s11661-021-06482-4.

[10] David. A. Porter, Kenneth E. Easterling, and Mohamed Y. Sherif, *Phase Transformations in Metals and Alloys*, 3rd ed. CRC Press, 2014.